



# Point cloud 3D parent surface reconstruction and weld seam feature extraction for robotic grinding path planning

Xiangfei Wang<sup>1</sup> · Xiaoqiang Zhang<sup>1</sup> · Xukai Ren<sup>1</sup> · Lufeng Li<sup>1</sup> · Hengjian Feng<sup>1</sup> · Yanbing He<sup>2</sup> · Huabin Chen<sup>1</sup> ·  
Xiaoqi Chen<sup>1,3</sup>

Received: 19 November 2019 / Accepted: 17 January 2020 / Published online: 20 February 2020  
© Springer-Verlag London Ltd., part of Springer Nature 2020

## Abstract

High-performance components with complex geometries make it difficult to determine the position and orientation of grinding tool. In this work, a fast and accurate robotic grinding path planning method is proposed for automatic removal of irregular weldments on a free form surface. The surface of workpiece is digitalized by 3D profile scanner and represented by point cloud data. Statistic filter, weighted least square regression and differences of normal vectors are used for point cloud pre-processing and segmentation. All segments are then modelled by B-spline surfaces to obtain the parent surface. A new superposition method is proposed to create a computer-aided design (CAD) model of the actual workpiece by adding the weld seam to the parent surface. The CAD model is then imported into an off-line simulation system to generate and execute grinding path. With the superposition method, the heights and widths of weld seam are extracted by analysing the difference between point cloud data and the reconstructed parent surface in order to determine the feed rate and size of grinding tool. Experimental results show that the proposed superposition method has the maximum absolute percentage error 5.3% and 41% saving in computation time in comparison with the conventional reverse engineering method.

**Keywords** Point cloud · Robotic grinding · 3D surface reconstruction · Weld seam · Path planning

## 1 Introduction

Grinding technology is of critical importance in modern manufacturing including ultra-high precision polishing [1] and hard-to-machine nickel-based super alloy processing [2]. Many efforts have been made for better understanding of the dynamics of the process including lubrication [3–8], abrasive grain interaction [9, 10], deformation field simulation [11] and

acoustic signal monitoring [12, 13]. These studies of grinding process contribute to broad applications of grinding technology [14]. One is the removal of excessive weld on surface of workpiece.

The workpiece after grinding of weld has smooth surface, high precision and even enhanced performance. For example, in automobile industry, the oil tanks of motorcycle need to stay in close contact with the rider. In order to avoid scratches with skin, the weldment must be grinded out. In chemical industries, the weld of pressure vessel must be grinded to certain shape to improve the durability of joint under corrosive environment [15]. In aerospace industries, small workpieces made from titanic alloy must meet the precision requirements by grinding out the excessive weld. The grinded weld has additional benefit of prolonged service time [16]. Furthermore, in jet engine turbine remanufacturing [17], the repaired turbine vanes must be grinded to the original shape by removing excessive weld. As can be seen, with the worldwide booming of high-end manufacturing, the market for grinding of weld is also large. Conventionally, weldment grinding is carried out manually due to the complex geometries of workpieces and process dynamics. However, the

✉ Huabin Chen  
hbchen@sjtu.edu.cn

Xiaoqi Chen  
xiaoqichen@swin.edu.au

<sup>1</sup> Shanghai Key Laboratory of Materials Laser Processing and Modification, School of Materials Science and Engineering, Shanghai Jiao Tong University, Shanghai 200240, People's Republic of China

<sup>2</sup> Guangzhou Rison Intelligent Technology Holding Co. Ltd., Guangzhou, People's Republic of China

<sup>3</sup> Faculty of Science, Engineering and Technology, Swinburne University of Technology, Hawthorn, Australia

manual grinding task is labour intensive and harmful to health. To free the operator from such a labourious task, robotic grinding [18–22] is introduced as an attractive alternative due to its higher accuracy and unrelenting repetitiveness.

One of the most important procedures in robotic weldment grinding is planning of the tool path that guides the motion of grinding tool to selectively remove excessive weld material on the workpiece. Many strategies for grinding tool path planning have been developed. One of them is generating the grinding path using the design data of the workpiece [23]. The most commonly used design data is CAD model. Wang et al. [24] sliced the CAD model to find the optimal contact points and tool orientations. Bian et al. [25] applied an off-line CAD-based path planning method for surface polishing of golf club head. However, these methods did not consider the defective areas of actual workpieces and were mostly used to polish the entire surface. Therefore, some researchers planned the grinding paths based on reconstructed models of the workpieces using reverse engineering. Huang et al. [26] first proposed a smart robot grinding system based on measured profiles for jet turbine vanes. Yilmaz et al. [27] proposed a recontouring method for jet engine turbine tips based on point cloud data obtained from non-contact measurement. Li [28] implemented a reverse engineering approach to polish workpieces with complex geometry. Wilson [14] used Boolean difference between the original defective model and the reconstructed model to create a parametric representation for the repair area.

Although reverse engineering methods have frequently been explored, there are still some limitations for applications. Firstly, the reported methods for reverse engineering are very complicated and difficult to implement [28]. Secondly, the computation for point cloud data and B-spline surface modelling is time consuming, and cluster computers have to be used to obtain a high-quality model at a reasonable speed.

In order to improve the efficiency, Zhang et al. [29] have proposed a direct method for slicing point cloud data based on octree search. The positions and orientations of the grinding tool are estimated by principal component analysis (PCA) of N-nearest neighbours of point cloud data. Li et al. [30] used a two-dimensional linear interpolation method to fit a fraction of point cloud data directly. The path was then planned using the locally fitted surface. However, direct processing of point cloud cannot obtain an analytical model about the object, thus has less accurate estimation of normal vectors and curvatures.

In order to overcome the limits of the current methods, here we propose a much more quick and accurate solution for grinding path planning. The overall procedure is shown in Fig. 1. Firstly, a non-contact measurement method based on 3D laser profile scanner is used to obtain the point cloud data of the region of interest (ROI) of workpiece. If the workpiece is new, B-spline modeling is used to construct the parent surface via point cloud data. Secondly, the weld seam features are extracted by comparing the deviations of point cloud with

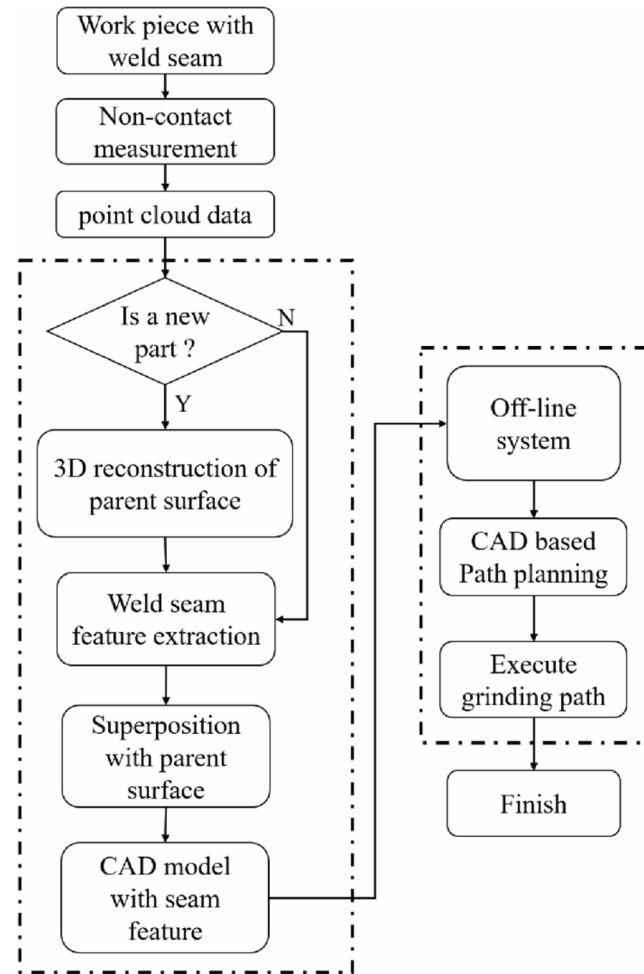


**Fig. 1** Schematic diagram of the parent surface and weld superposition method for grinding path planning

parent surface. Then, the extracted features of weld seam are superimposed on the parent surface to create CAD model of the actual workpiece. Lastly, the obtained CAD model is imported to an off-line path planning system which can automatically generate the grinding path.

## 2 Experiments and methods

### 2.1 Experimental setup

The workpiece used in this study is oil tank made from two stainless steel shells that are joined by welding along the centreline. The shape of the oil tank is a free form surface which makes the path planning very difficult. To be specific, some part of the free form surface has large curvatures that make the orientation of the grinding tool hard to determine. Thus, to accurately calculate the orientation of the grinding tool, an explicit model of the surface near the weld seam is necessary.

In order to improve the efficiency, surface near the weld seam is considered as region of interest (ROI) as shown in Fig. 2a. The surface is digitalized by a Keyence LJ-V7080 laser scanner (Fig. 2b) which collects the point cloud data. The laser beam which have wavelength of 405 nm spreads into a line after passing through the lens. When hitting the object, the laser line lights up one cross-section of the object's surface. Then, a charge-coupled device (CCD) camera is used to image the lightened profile of the object. During scanning, the 3D profile scanner is mounted at the end effector of robot arm. The robot arm moves along a predefined trajectory in the space. The point on the surface of workpiece can be measured based on triangulation measurement theory as shown in Fig. 2b. The height of surface H is calculated using the following equation:

$$H = \frac{l \cdot h}{\sqrt{d^2 + h^2} \sin(\theta)} \quad (1)$$

The computation platform for surface modelling is an industrial computer with an Intel Core i5-6500 processor. The size of random-access memory is 8 GB. The operation system is Windows 10. The programming language is C++. The development environment is visual studio 2017 community edition. After point cloud processing and surface modelling, a CAD model of the ROI is obtained and imported into an off-line simulation environment.

The off-line simulation environment is Robot Studio software, the configuration of the off-line system is the same as the actual laboratory environment. Once the grinding path has been planned, the trajectory of path is uploaded to an ABB IRB\_6700\_200\_260 robot to execute the grinding task. To conform to the complex geometry of the oil tank surface, the grinding tool used here is a self-designed compliant grinder driven by force feedback control system. The diameter of the flap disc is 115 mm and the abrasive grit size is 0.250 mm. To

obtain high surface quality, the weld seam is removed in multiple rounds of grinding. In addition, complex S-shape weld seam is used to test the robustness of proposed method. Finally, six test blocks with known heights and widths are used to verify the accuracy and repeatability of the method quantitatively.

## 2.2 Point cloud data acquisition

In order to ensure the accuracy of measured point cloud data, the hand-eye relationship between the laser scanner and robot end effector is calibrated using the method described in [31]. The rotation and translation parts of the hand-eye matrix are obtained by first fixing and then varying the orientation of robot end effector. To reduce the calibration error, multiple measurements are carried out. The rotation parts of hand-eye matrices are converted to quaternions and then taken average which is finally converted back to matrix representation. Based on the rotation matrix, the translation part is solved by the least square method.

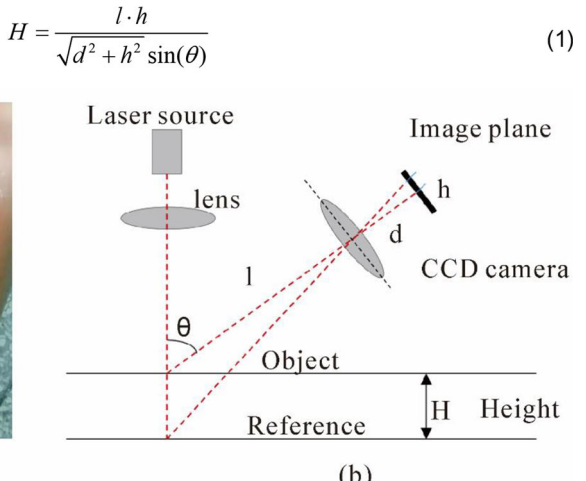
The point cloud data obtained by non-contact measurement has 200,000 scanning points that are stored in a two-dimensional (2D) matrix. Each value is a measurement of the height of the surface. The row of the matrix corresponds to a single scan line and different rows correspond to scan lines obtained at different time. The distance ( $\Delta y$ ) between adjacent rows of data is determined by the speed of end effector. The distance ( $\Delta x$ ) between two adjacent points in a row is determined by the sampling frequency of the equipment. The measured height  $H$  is the value of z coordinate. In order to convert 2D matrix of heights into 3D Cartesian coordinate (x, y, z), the following equations are used.

$$\begin{aligned} x &= c\Delta x \\ y &= r\Delta y \\ z &= H_{r,c} \end{aligned} \quad (2)$$

**Fig. 2** Scanning of ROI based on triangulation measurement theory. **a** The region of interest. **b** Schematics of triangulation measurement theory



(a)



(b)

where  $r$  is the number of rows and  $c$  is the number of columns in 2D matrix.

### 2.3 Parent surface reconstruction

The raw point cloud data contains much noise that must be removed. There are various sources for noise, including reflection of light, complex geometries and mechanical vibrations. Among them, the most significant factor is reflection of light caused by scratches on the surface, just as shown in Fig. 3. The scratches expose the silver colour of the base metal and have very shiny appearances under the laser beam light. Since the shiny base metal reflects most of the light, the measured point data around those scratches is very unreliable.

In addition, complex geometry is also a main source of error. Since light always travels along a straight line, weld seam with complex shape on the surface will block the passage of light and create small shadows which can induce significant errors for measured point data. To illustrate the influence of shadows, a complex S-shape weld seam is created on the surface of oil tank. Furthermore, the height of the S-shape weld seam is two times higher than a normal weld seam. Thus, the shadows around the weld seam are more prominent.

In order to reduce the error of measured point cloud data, the outliers must first be removed and the voids left must be filled. There are many methods to remove the outliers. Some [32, 33] are fast but less accurate, while others are more accurate but slower [34, 35]. We use a statistic filtering [36] method to improve the accuracy. During statistic filtering, 20 nearest neighbours are found for every point. The mean distance between selected point and 20 neighbouring point is calculated. Points with mean distance larger than predefined threshold are trimmed out from point cloud data. Figure 4 shows the point mean distance before and after removing outliers.

**Fig. 3** Scratches on the surface on oil tank. **a** Overview of scratched oil tank. **b, c** Zoom-in view of **a**

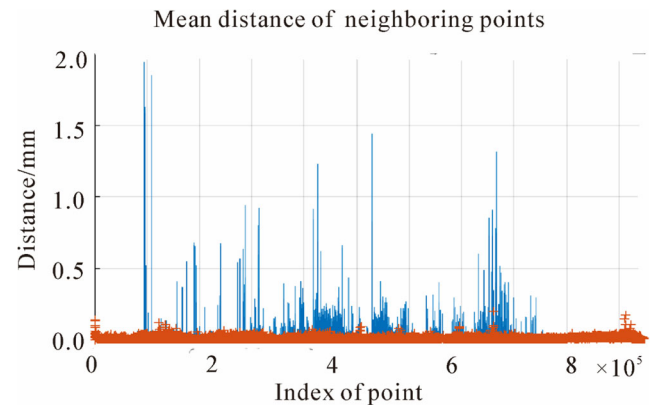
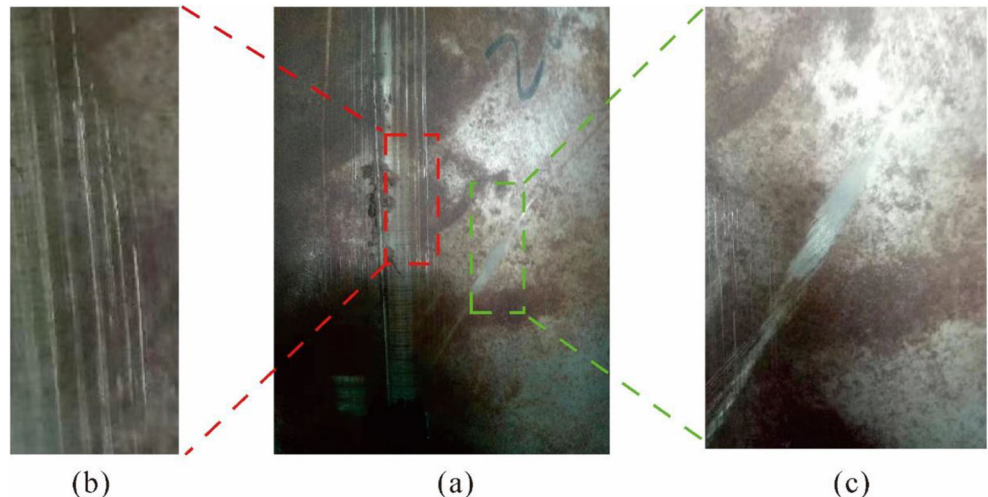
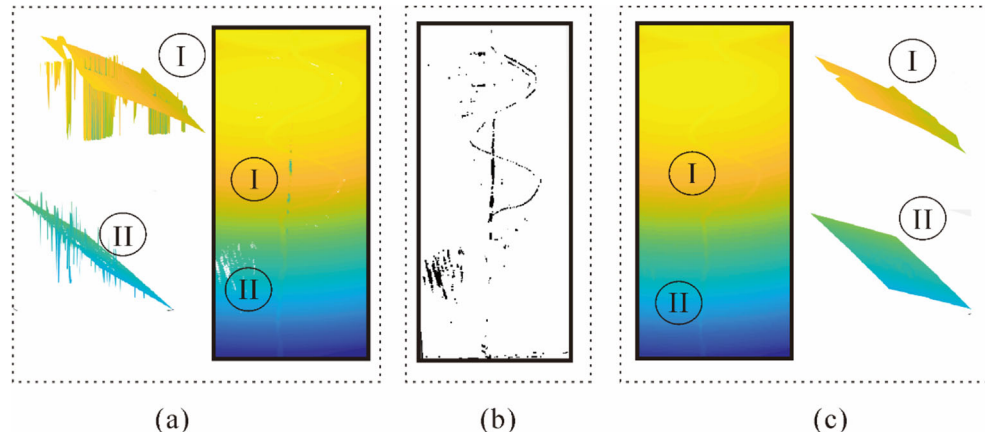


**Fig. 4** The mean distance of every points with 20 of its neighbours. The blue and red colours represent the data before and after filtering

To obtain a complete set of point cloud data for a freeform surface, the voids of removed outliers have to be filled. In addition, the newly filled points in the voids must agree with the geometry of the original surface. To achieve this, a boundary propagation method is used. During boundary propagation, only the pixels on the boundary are filled by the mean value of four nearest neighbours. Thus, the void pixels are filled iteratively with the gradual propagation of their newly filled boundary. For each iteration, the boundary always represents a smooth transition from the original data to the center of void. Hence, the filled data conforms to the original geometry of the surface.

The effects of statistic filtering and boundary propagation are illustrated in Fig. 5. The original point cloud before pre-processing is shown in Fig. 5a. In particular, the region (I) corresponds to the noise caused by shadows due to complex S-shape weld seam. The region (II) illustrates noise caused by reflections of light from small scratches. The voids caused by removing outliers are shown in Fig. 5b. The final point cloud after filling voids is shown in Fig. 5c, which exhibits a relatively smoothed surface.

**Fig. 5** Removing and filling outliers in point cloud data. **a** Original point cloud data, (I) and (II) zoom-in views of points with significant errors. **b** Voids left after outliers are trimmed. **c** Final point cloud after trimming outliers and subsequent filling of the voids



Although statistic filtering and boundary propagation methods are very efficient to remove outliers, there are still some small random noises, which are caused by diffraction of light on the surface. As have been studied in [37], those diffraction errors obey the Poisson distribution. For every point  $(x, y, z)$ , the error of diffraction is denoted as  $(x + \varepsilon, y + \varepsilon, z + \varepsilon)$ , where  $\varepsilon$  represents a small random variable.

To reduce the small random noise, a non-parametric method based on weighted least square (WLS) regression [38] is used in this work. The weight of the WLS is a Gaussian function shown as follows.

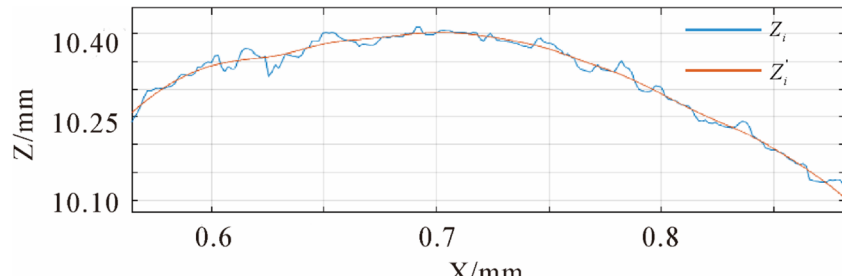
$$w(x-x_i) = \begin{cases} \frac{e^{-(\|x-x_i\|/\alpha d)^2}-e^{-1/\alpha^2}}{1-e^{-1/\alpha^2}} & \text{if } \|x-x_i\| \leq d \\ 0 & \text{else} \end{cases} \quad (3)$$

where  $\alpha$  denotes the width of weight function. The template for regression is a first-order polynomial  $z = ax + b$ .  $(x_i, z_i)$  are series of data points for a single scan. The coefficients  $a$  and  $b$  are calculated by solving the following set of equations via least square method.

$$w(x_i-x_k)(ax_i-b) = w(x_i-x_k)z_i \quad i = k-n/2, \dots, k+n/2 \quad (4)$$

Then, the modified value  $z'_k$  is expressed as  $z'_k = ax_k + b$ . Thus, the new point  $(x_k, z'_k)$  has smaller error compared with the original data. Figure 6 shows the points before and after WLS filter.

**Fig. 6** A single scan line of point cloud data filtered by WLS method. The blue and red colours represent the data before and after filtering



After filtering out all the noise, segmentation of point cloud follows. As shown in Fig. 7, the surface of point cloud is segmented into smaller patches by intersection lines. Thus, the intersection lines must first be found, which is achieved by analyzing differences of normal (DON) vectors [39].

The procedures of finding intersection lines from DON are illustrated as follows. Firstly, the normal vectors are estimated using PCA method which is shown in Fig. 7 a. Then, DON at each point is calculated as illustrated in Fig. 7 b. Specifically, the DON along X direction is defined as  $|\overrightarrow{N_{i+1,j}} - \overrightarrow{N_{i,j}}|$ . The calculated value is stored in a 2D matrix which looks like an image (Fig. 7c). Similarly, the DON along Y direction is calculated as  $|\overrightarrow{N_{i,j+1}} - \overrightarrow{N_{i,j}}|$  and the corresponding image is shown in Fig. 7 d. The index  $i$  and  $j$  represent the row and column of scanned point cloud data. As can be seen, the DON along the X direction has large values near the weld seam; hence, DON along X direction is used to extract the weld seam. In addition, the DON along Y direction has large values near the intersection lines; thus, DON along Y direction is used to extract the intersection lines.

Further details to extract intersection lines and weld seam are demonstrated in Fig. 8. The DONs are first filtered by Gaussian filter. Then, a dynamic threshold method is implemented to segment the image into ROIs and background (Fig. 8a). The ROIs are morphologically opened and then closed [40] to make the target regions connect into a large ROI (Fig.

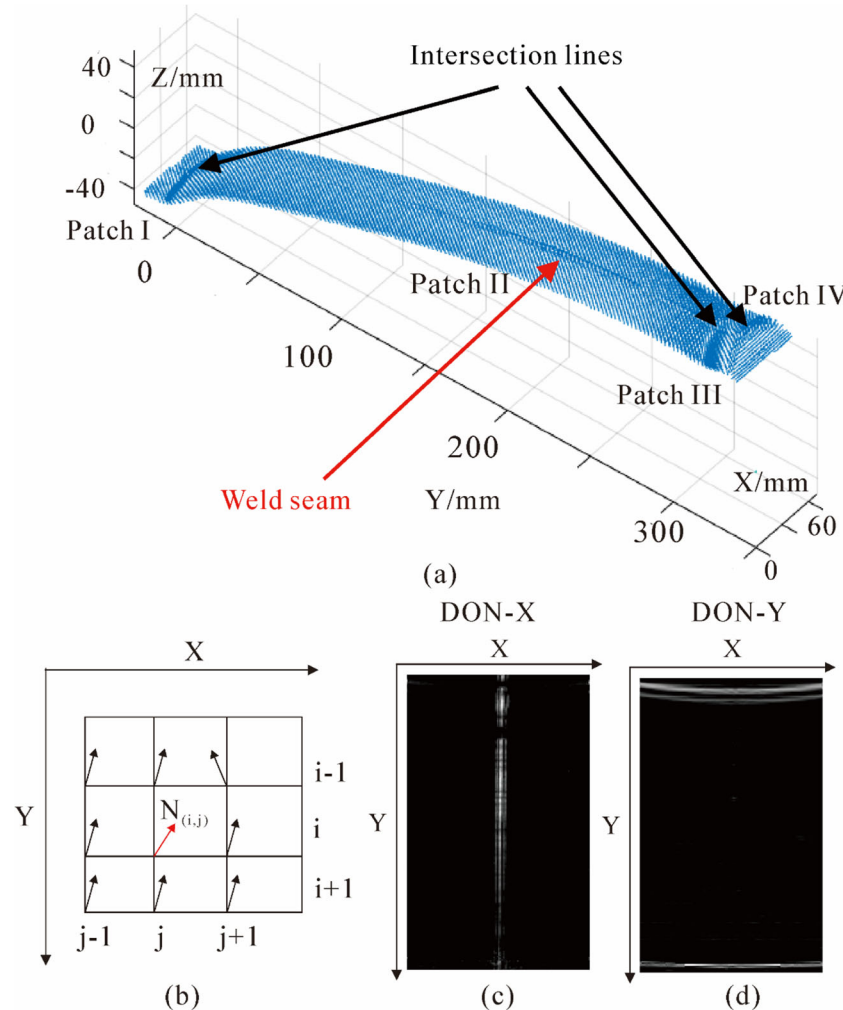


**Fig. 7** Find intersection lines using DON. **a** Estimation of the normal vectors of point cloud data using PCA analysis. **b** Definition of DON. **c** DON along X direction. **d** DON along Y direction

8b). As shown in Fig. 8 b, the large vertical ROI represents points on weld seam. To construct parent surface without weld seam, the points on weld seam are trimmed out and the voids are then filled by boundary propagation algorithm described earlier. Then, the sporadic ROIs with area smaller than 30 pixels are discarded because they represent noise in the image. Finally, the weld seam and intersection lines are extracted by implementing Gaussian line detection method on selected ROI [41–43] (Fig. 8c).

In order to simplify the problem, the segmentation is first carried out in 2D X-Y plane. Then, all points in 2D are conveniently converted back to 3D using Eq. (2). To segment the point cloud in 2D, the extracted intersection lines are used as partition lines which divide the 2D plane into several regions. The points within each region are then filled by continuous transformation of opposite sides. Figure 9 shows the segmentation process in 2D. First, the ending points of partition lines are found by scanline algorithm [44]. Then, each region is defined using partition lines between two ending points as its outer-boundaries.

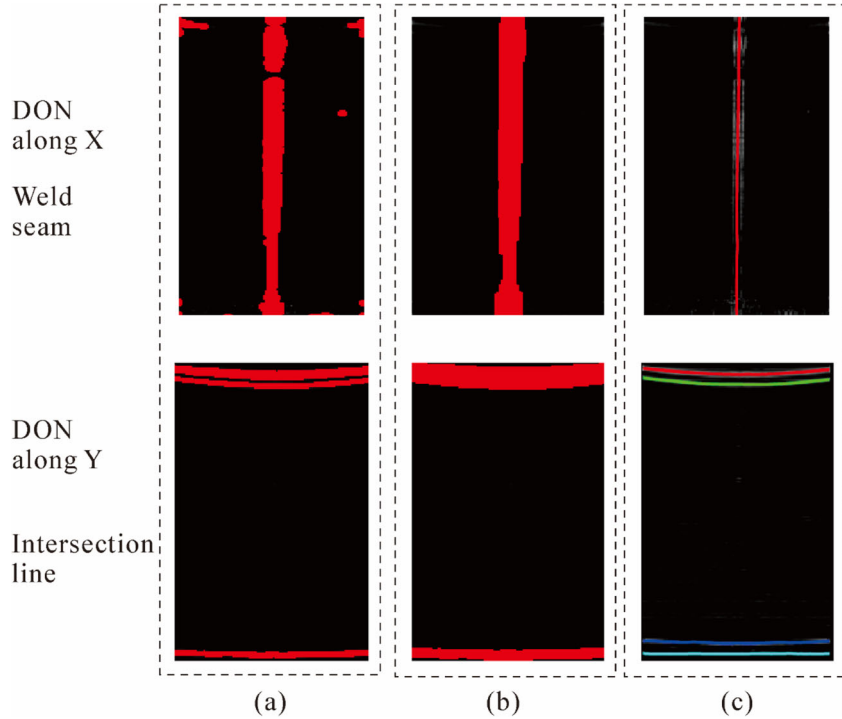
After finding the outer-boundaries, the exact location and geometry of the region are obtained. However, to completely describe 3D surface, the inner points of each region need to be filled. The filling process is based on continuous transformation of opposite sides which is illustrated in Fig. 10 b–d.

First, the number of points on the two opposite sides of the original four-side region needs to be normalized to the same. For example, in Fig. 10a, the number of points on L1, L2, L3 and L4 are 7, 3, 2 and 2, respectively. After normalization, the number of points on L1 and L3 is 4 and the number of points on L2 and L4 is 7 (Fig. 10b).

Second, series of transition lines (Fig. 10c) are created continuously between the longer side pairs according to Eq. (5).

$$\begin{aligned} \frac{P_r^c - P_r}{P'_r - P_r} &= \frac{l_1}{l_0} = v^c \\ \frac{S_1}{S_0} &= u^r \end{aligned} \quad (5)$$

**Fig. 8** Find intersection lines and weld seam using DON, represented by horizontal curve and vertical lines, respectively. **a** Dynamic thresholding. **b** Morphological open and then close. **c** Gaussian line detection



Third, those transition lines are linearly stretched and shifted according to the Eq. (6), to make sure the two ending points of transition lines overlap with the points on the short side pairs

$$k = \frac{|q_c - q'_c|}{|p_1^c - p_n^c|} \quad (6)$$

$$p_r^c = (p_r^c - p_1^c)k + q_c \quad r = 1 \dots n$$

where  $k$  is the ratio of stretching.  $p_r^c$  are the points on continuous line,  $q_c$  and  $q'_c$  are the two points on the short side pairs. After filling inner points, the segmented 2D regions together with inner points are shown in Fig. 11a.

To obtain an explicit representation of the parent surface, B-spline model is used curve fitting. The B-spline model [45] includes knot vectors, control points and parameterized coordinates of 3D point. To reduce the fitting errors of B-spline model, we propose a new self-consistent optimization algorithm as

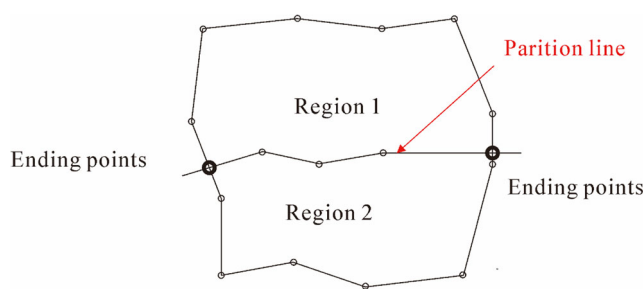


**Fig. 9** Find ending points of Partition lines

shown in Fig. 12. First, the parameterized coordinate  $(u^r, v^c)$  of point cloud data is initialized by Eq. (5). Second, the control points of B-spline surface are calculated by least square method. Third, the control points are used to obtain an explicit parameterized function of B-spline surface  $Z^i(u, v)$ .

Based on explicit expression of the surface, The optimization of parameterized coordinate  $(u^r, v^c)$  is carried out in two steps.

The first step is to calculate the deviation with parent surface for every parameterized point  $(u^r, v^c)$

$$E^i = Z^i(u^r, v^c) - Z_{r,c}^i \quad (7)$$

where  $Z_{r,c}^i$  is the measured point,  $Z^i(u^r, v^c)$  is the point on B-spline surface.

Then, the deviation vector is decomposed onto the small tangent plane which is spanned by vector  $Z_u^i(u^r, v^c)$  and vector  $Z_v^i(u^r, v^c)$ .

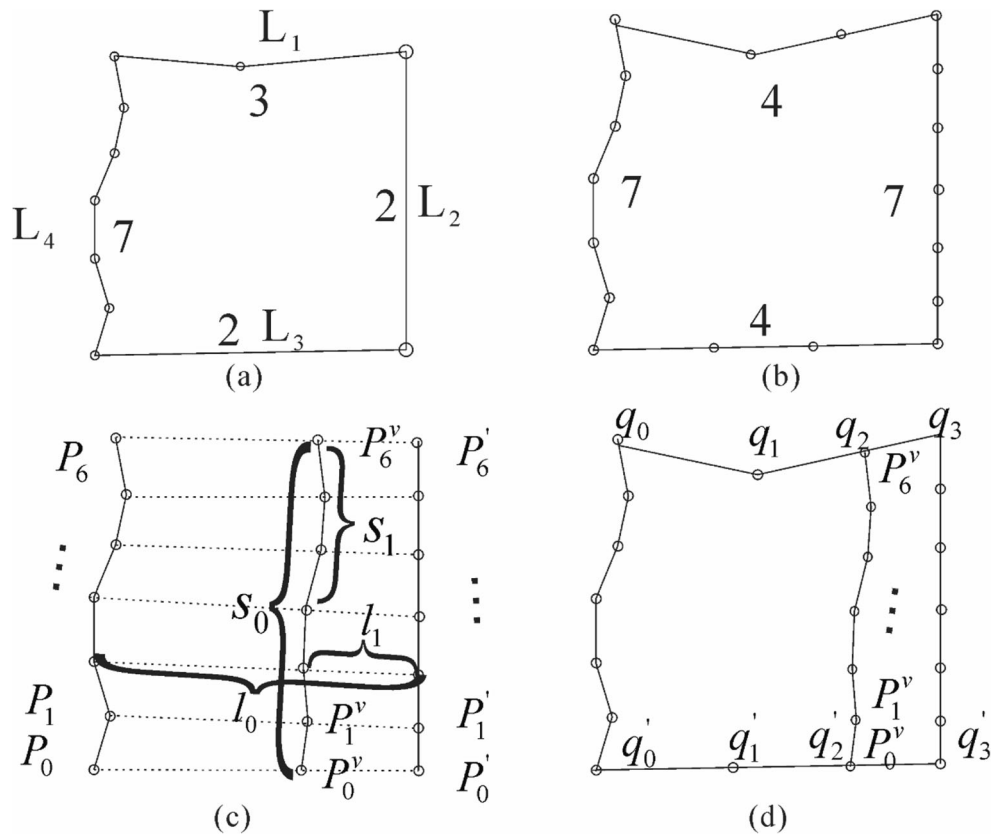
$$E_{\text{tangent}}^i = \Delta u Z_u^i + \Delta v Z_v^i = E^i - N^j E^j N^i \quad (8)$$

where  $N^j$  is the normal vector of the surface. Thus, the parameterized coordinate  $(u^r, v^c)$  is optimized iteratively by the following equations.

$$\begin{aligned} u^r &= u^r + \Delta u \\ v^c &= v^c + \Delta v \end{aligned} \quad (9)$$

The second step is to reduce the error of the knot vectors. For B-spline surface, there are two independent knot vectors,

**Fig. 10** Schematics of filling inner points by continuous transformation. **a**  $L_1, L_2, L_3, L_4$  are four sides of the original boundaries. **b** Normalization of the number of points on opposite sides. **c** Continuous transition line of side pairs. **d** Fill the inner region by stretching and shifting of the transition line

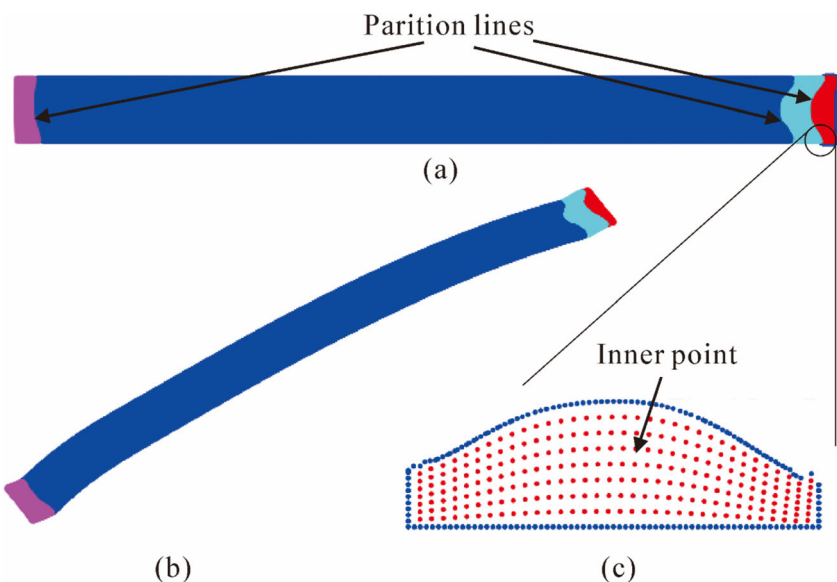


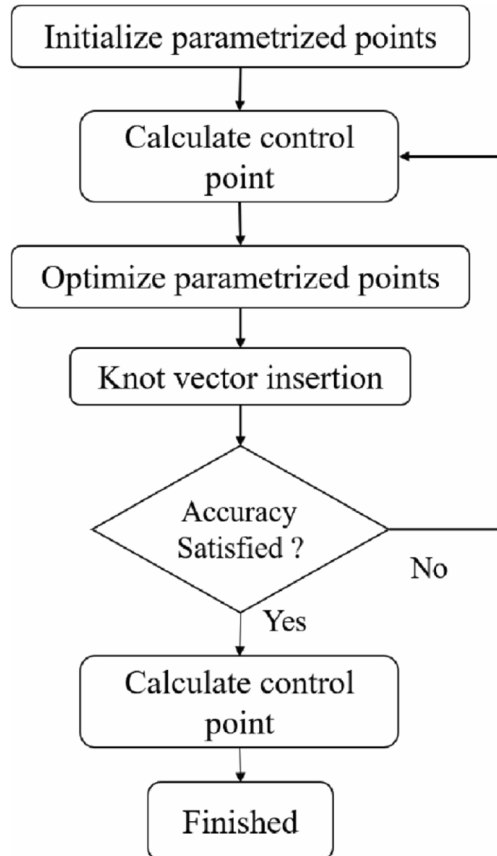
namely,  $U = \{0, \dots, 0, u_{p+1}, \dots, u_n, 1 \dots 1\}$  and  $V = \{0, \dots, 0, v_{p+1}, \dots, v_n, 1 \dots 1\}$ . The error for knot point  $u_i$  is the average error ( $E_i$ ) of points that lay within the interval  $u_i$  and  $u_{i+1}$ . During each iteration, the knot that has the biggest error ( $E_i^u$ ) is selected and a new knot is inserted at the interval  $u_i$  and  $u_{i+1}$ . The same operations are carried out in knot vector  $V$ .

If the error  $E_i^u$  and  $E_i^v$  are smaller than globally defined threshold, finish the insertion process, else repeat the above-mentioned process. Table 1 demonstrates the reduction of  $E_i^u$  and  $E_i^v$  for 6 iterations and shows fast error convergence.

To obtain the parent surface, the self-consistent optimization is applied to each segment of the point cloud to obtain

**Fig. 11** Segmentation of point cloud data. **a** Final segmented regions in 2D with inner points already filled. **b** Mapping 2D points to 3D points using Eq. (2). **c** Zoom-in view of a four-edge region filled by continuous transformation



**Fig. 12** Schematics of self-consistent optimization

series of B-spline patches as shown in Fig. 13. After self-consistent optimization, the control points and parameterized coordinates of a single patch are shown in Fig. 13a. The patch is made by B-spline curves which describe the boundary, and a B-spline surface which describes the main part of the patch (Fig. 13b). After combining all small patches, a complete parent surface can be obtained (Fig. 13c).

#### 2.4 Weld seam feature extraction and superposition

The features of weld seam include the centerline, height, width. To extract the weld seam features, the deviations (Eq. (7)) of point cloud with respect to the parent surface are calculated as shown in Fig. 14a. The centerline of weld seam is extracted by analyzing the deviations using image processing methods mentioned in Sect. 2.3. The width and height of weld seam are defined as average values over fixed interval (Fig. 14a). In order to combine weld seam with the parent surface, the point cloud data is segmented again by weld seam centerline (Fig. 14b). The new segments are then fitted by self-consistent B-spline method mentioned above. Finally, the weld seam centerline is added to the parent surface as shown in Fig. 14c.

**Table 1** Fitting errors of self-consistent optimization

Iterations	Fitting errors		
	$E_i^u$ /mm	$E_i^v$ /mm	Mean/mm
1	0.54	0.88	0.71
2	0.34	0.57	0.46
3	0.10	0.17	0.14
4	0.08	0.10	0.09
5	0.05	0.07	0.06
6	0.05	0.06	0.06

The obtained B-spline parent surface and weld seam features are used to construct a CAD model according to ISO 10303-21. In this standard, the parent surface is defined as a shell. The patches are represented by advanced surfaces that are combined into the shell. The advanced surface is made up by face boundaries and B-spline surface. The final CAD model is output to a .STP file in the Standard for the Exchange of Product Data (STEP) format.

#### 2.5 Integration with off-line system

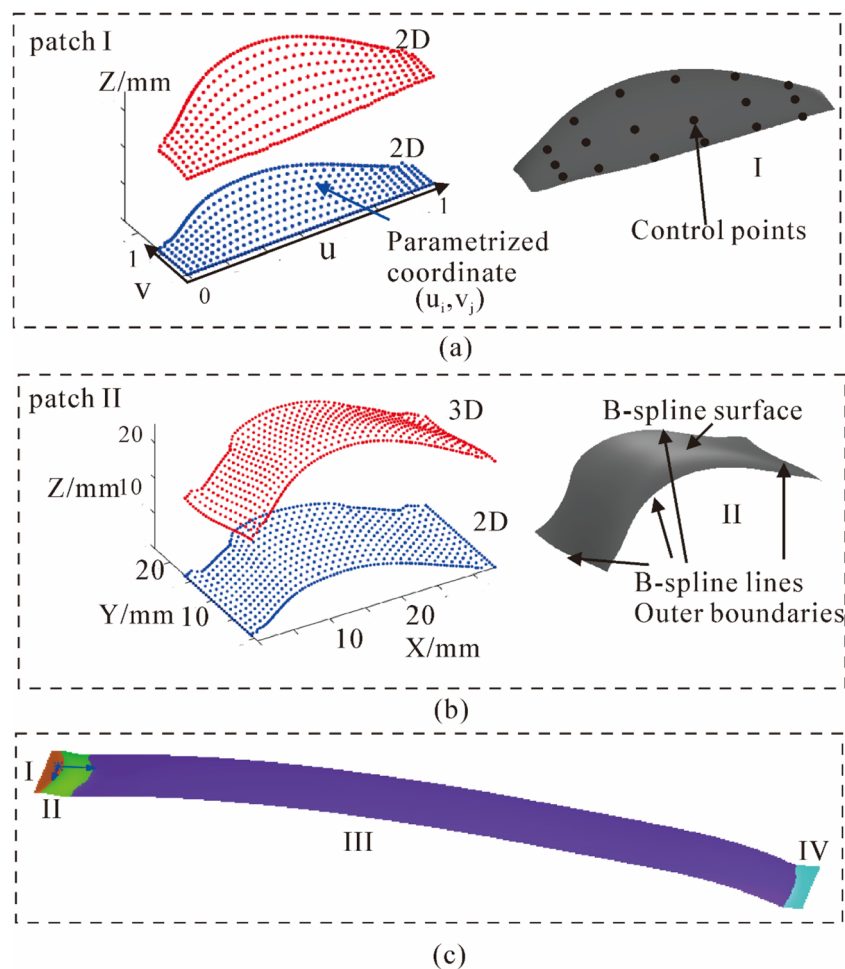
When the CAD model is imported into the off-line simulation system, the grinding tool is positioned at one ending point of the weld seam. Then, the system can automatically track the weld seam and generate the grinding path. In order to achieve optimal contact between the grinding tool and the weld, the contact points are defined on the centerline of weld seam. The distance of two adjacent contact points is optimized based on the curvature of surface. The orientation of the tool is determined by surface normal vector and the tangent direction of the weld seam. As shown in Fig. 15c, the grinding tool path achieves optimal contact with the workpiece, indicating that the reconstructed surface has very high quality.

### 3 Results and discussion

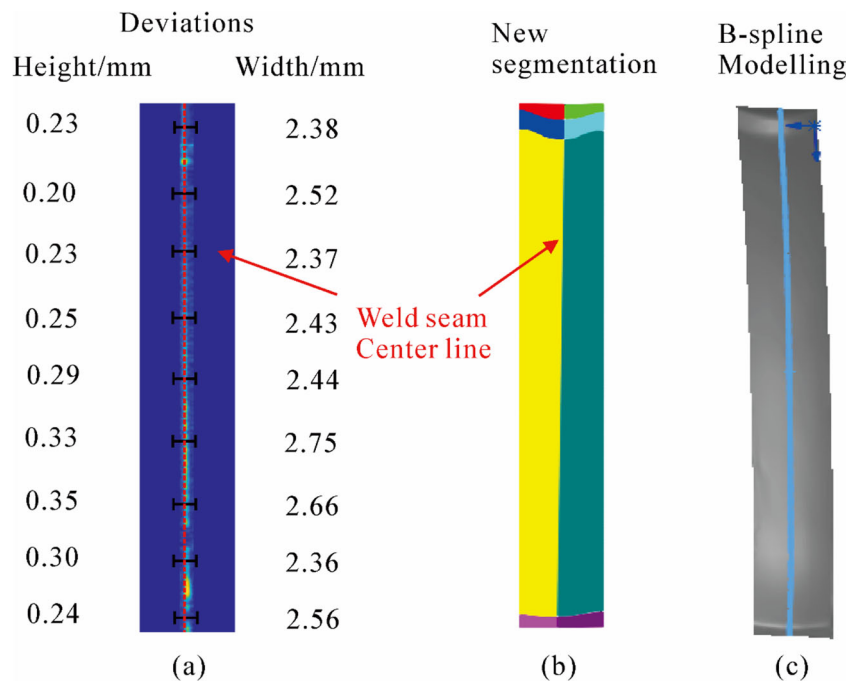
#### 3.1 Grinding of oil tanks

Experimental work was conducted to validate the proposed surface reconstruction and weld seam superposition method, and to test the generated grinding tool path. Firstly, the position of the oil tank in world coordinate was calibrated as configured in the simulation environment. Secondly, the simulated grinding tool path was uploaded to the controller of the robot that executes the grinding task. To obtain higher surface integrity, the grinding process was conducted in multiple rounds. The height of the weld seam was used to optimize

**Fig. 13** B-spline model obtained by self-consistent optimization. **a** Parameterized coordinates and control points after self-consistent optimization for patch I. **b** Model of patch II. With the boundary defined by B-spline lines and the surface of patch defined by B-spline surface. **c** The final parent surface obtained by combining all small patches



**Fig. 14** Superposition of weld seam with parent surface. **a** Deviation of point cloud from parent surface. **b** New segmentation of point cloud data using weld seam centerline. **c** B-spline model of workpiece superposed with the weld seam represented by the centerline



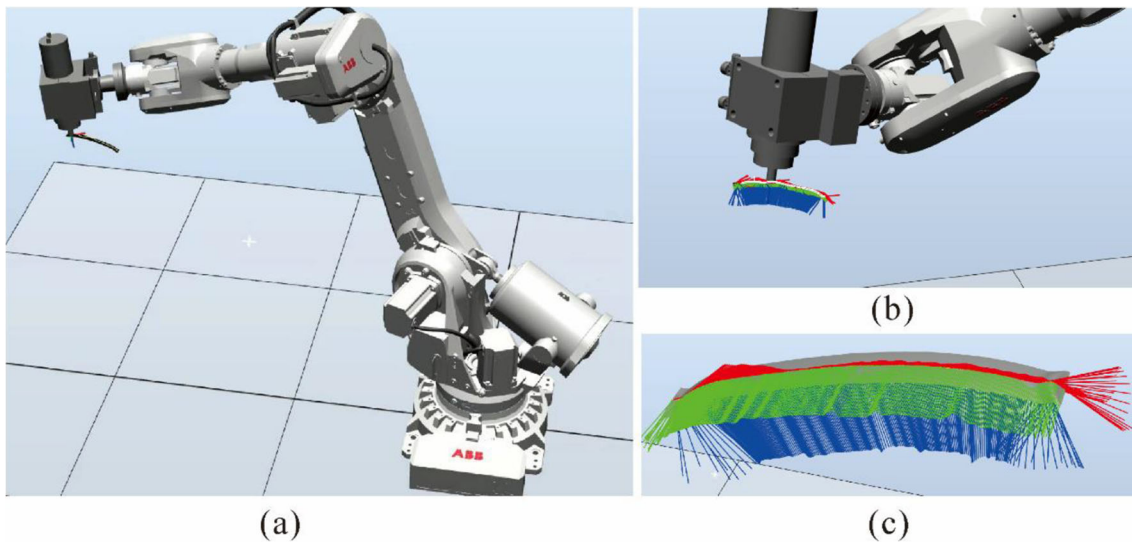


**Fig. 15** Off-line simulation environment for grinding path planning. **a** Robotic grinding system. **b** Execution of grinding task. **c** Automatic generation of grinding tool path, including the normal vector of the

surface (blue), the tangent direction of weld seam centerline (red) and the cross product of normal vector and tangent vector (green)

the feed rate at each round of grinding. The width of the weld seam was used to determine the size of the flap disc. The detailed parameters for grinding are illustrated in Table 2. The appearances of straight weld seam before and after grinding are shown in Fig. 16.

To test the robustness of the method, the grinding of a more complex weld seam with S-shape is conducted, the original tank is shown in Fig. 17 a. For one aspect, the point cloud of S-shape weld seam always contains more noise which is caused by blocking of light. In addition, the S-shape partition line increases the complexity of B-spline modelling. Despite so many difficulties, the proposed superposition method can still reconstruct the CAD model and plan the grinding path successfully. Figure 17 b shows the intermediate results for different procedures of superposition algorithm. The obtained CAD model with S-shape weld seam is used by the off-line system to generate the grinding tool path. It can be seen that the grinding tool path successfully maintains optimal contacts with the workpiece. Finally, the grinding tool path is uploaded to the robot controller that performs the grinding task. The grinding parameters are the same as defined in Table 2. The oil tank after grinding is shown in Fig. 17c.

**Table 2** Grinding parameters for oil tanks

Rounds	Feed rate/mm	Contact force/N	Speed/RPM
1	0.56	40	600
2	0.28	30	600
3	0.11	20	600

### 3.2 Computation efficiency

In order to have a detailed comparison between the conventional reverse engineering method and the proposed surface

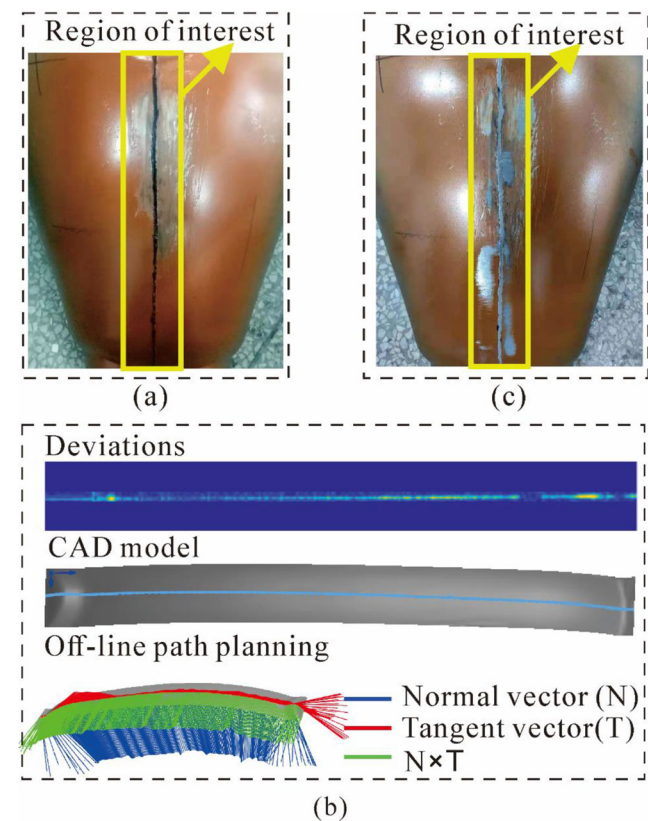


**Fig. 16** Grinding of weld seam. **a** Weld seam before grinding. **b** Intermediate results for path planning. **c** Weld seam after grinding

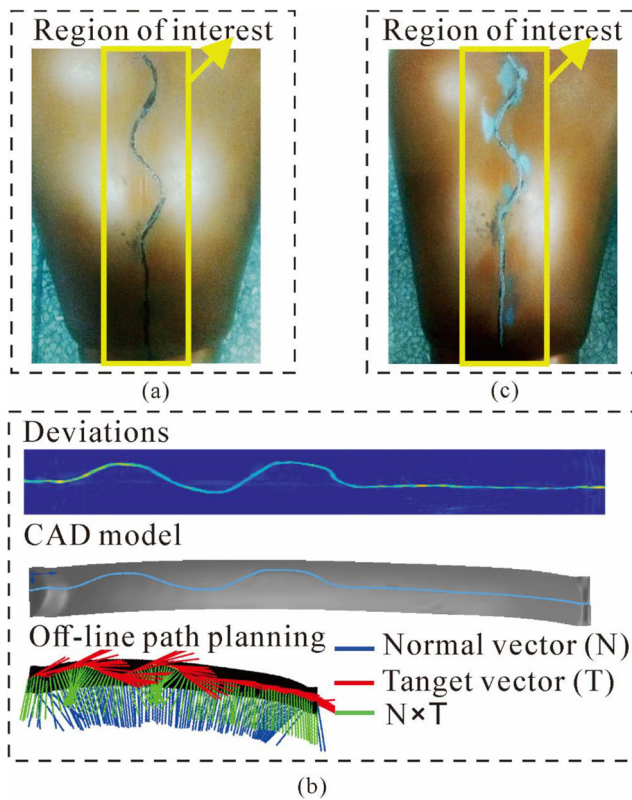


**Fig. 17** Grinding of oil tank with complex S-shape weld seam. **a** The original oil tank with S-shape weld seam. **b** Intermediate results during path planning. **c** The final oil tank after grinding

reconstruction and superposition method, the time spent on various procedures of calculation is analyzed. The procedures to implement reverse engineering method are chosen from [46].

As shown in Fig. 18, filtering and PCA procedures are used only in reverse engineering method while deviation calculation is used only in our proposed superposition method. Other procedures including segmentation, B-spline modelling and

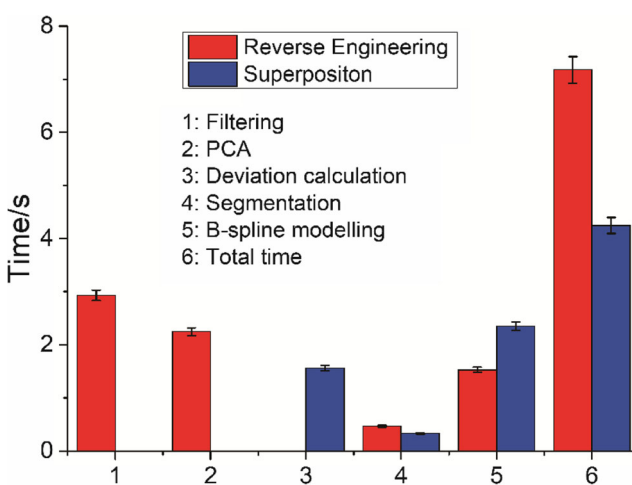


**Fig. 18** Time spent on different procedures for reverse engineering and superposition algorithm

self-consistent optimization are shared by two methods. The total run time for the superposition method is 4.24 s, which is much shorter than 7.16 s required by the reverse engineering method. The substantial computation time saving (41%) is because that the new reconstruction and superposition algorithm does not include filtering and PCA procedures that are needed by the reverse engineering method. Although the superposition method has additional deviation calculation, the computation is efficient. Thus, the experimental result shows that the superposition method significantly improves the speed of reconstruction by obviating filtering and PCA procedures.

### 3.3 Verification of accuracy and repeatability

To test the accuracy and repeatability of the algorithm, the exact height and width of the weld seam must be known. However, a weld seam with very accurate geometry is very hard to obtain. Thus, we used test blocks with known heights and widths. In this experiment, three test blocks with different heights 0.30 mm, 0.60 mm and 0.90 mm were used to test the measured heights (Fig. 19a). Three test blocks with different widths, 2.00 mm, 4.00 mm and 6.00 mm, were used to test the measured widths (Fig. 19b). The sampling frequency of the scanner is 62.5 kHz. The test blocks were placed on a curved surface. The speed of the robot end effector was set as 5 mm/s.

To measure the heights and widths of the test blocks, first, the parent surfaces are reconstructed. Then, the point clouds are projected to the parent surfaces to determine the deviations  $E^i$ . The deviations  $E^i$  equal to the heights of test blocks since the parent surfaces are smoothed. The width of curved surface which has large  $E^i$  is defined as the width of the test blocks. To reduce the measurement error, three cross-sections of the test blocks (Fig. 19) are analyzed. The heights for three test blocks are defined as the mean values of the three cross-sections. The measured heights for low, middle and high test blocks are 0.28 mm, 0.58 mm and 0.89 mm. The percentage of error are 4.4%, 2.2% and 1.4%, respectively. Similar analysis is carried out for test blocks with different widths. The measured widths of three test blocks are 2.11 mm, 4.07 mm and 5.98 mm. Hence, the percentages of errors are 5.3%, 1.7% and 0.3%, respectively, adequately small for robot grinding path planning. It should be noted that the overall error includes robot and sensor inaccuracies on top of the error resulting from the superposition algorithm. As such, the relative error for test blocks of smaller height and width is larger than that for test blocks with larger height and width. The results show that the proposed method is accurate and effective for extracting the heights and widths features of weld seam.

To verify the repeatability of the method, the same test blocks are scanned three times each. Then, three sets of cloud data are processed using the same proposed method. The measured results are shown in Table 3. As can be seen, the

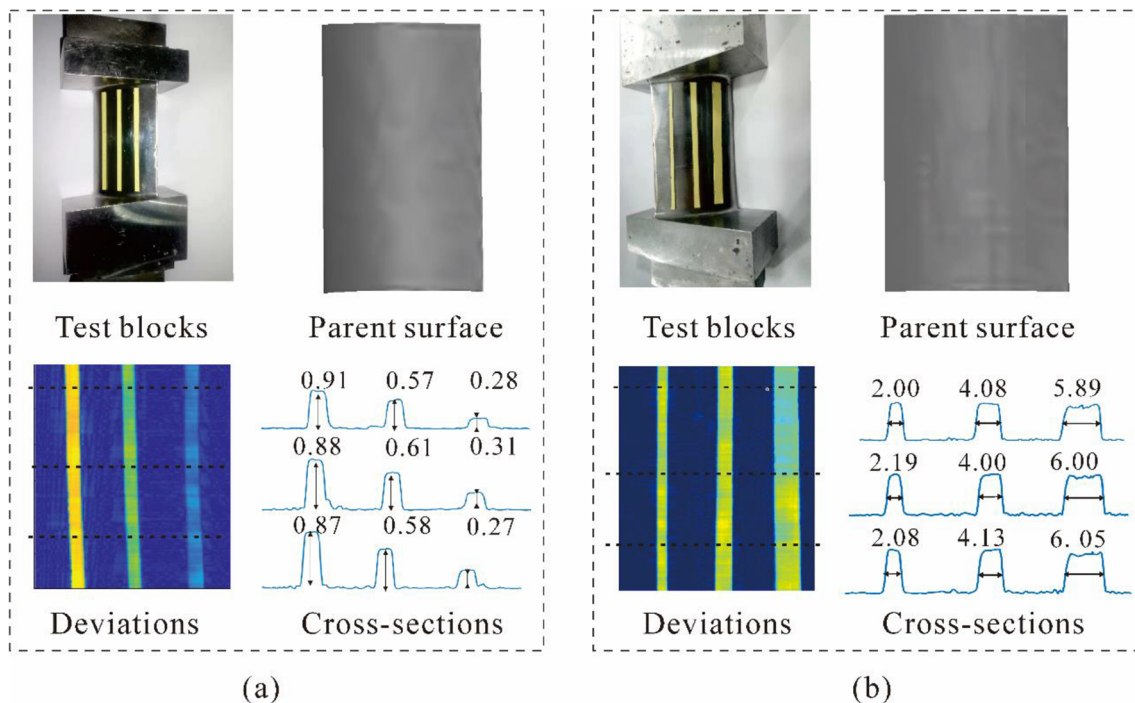


**Fig. 19** Accuracy and repeatability validation using test blocks with known heights and widths. **a** Test blocks with different heights. **b** Test blocks with different widths

systematic error defined as the mean measurement error indicates the proposed method tends to underestimate the actual heights of test blocks. However, this systematic error can be eliminated by careful calibration of the system. The standard deviation ranges from 0.01 to 0.5%, depending on the size of the feature measured.

Comparing the previous studies of contact measurement using a displacement probe, the repeatability [26] of the laser profile scanner is on the same level of accuracy which is 1  $\mu\text{m}$ . In consideration of robot deflection, calibration and scanner errors, the total repeatability of the system is 20  $\mu\text{m}$  which is smaller than 35  $\mu\text{m}$  as reported in other non-contact measurement methods [27]. Hence, the proposed method in this work for surface reconstruction and path planning is sufficiently accurate for most weldment grinding applications.

## 4 Conclusions

This work presents a novel path planning method for robotic grinding based on con-contact measurement of point cloud data. The parent surface of work piece is constructed by B-spline modelling. The features of weld seam are extracted by analyzing the deviations of point cloud with parent surface. CAD models of actual workpieces are reconstructed by superposition of the parent surface and weld seam feature. Then, the CAD models are imported into off-line path planning system to generate the grinding path. The accuracy and repeatability of this method are tested by multiple scans of the same test blocks with known geometry. The reconstruction errors are within 5.3% for the test blocks of varying sizes. In addition, the proposed method is more efficient for computation.

**Table 3** Repetitive measurements for the same test blocks against the real values

	Height			Width		
	Low/mm	Middle/mm	High/mm	Narrow/mm	Middle/mm	Wide/mm
Real value	0.30	0.60	0.90	2.00	4.00	6.00
Measurement 1	0.29	0.58	0.90	2.05	4.08	5.89
Measurement 2	0.28	0.60	0.88	2.19	4.00	6.00
Measurement 3	0.31	0.62	0.90	2.08	4.13	6.05
Mean values/mm	0.28	0.58	0.88	2.11	4.07	5.98
Standard deviation %	0.5	0.2	0.1	0.1	0.02	0.01
Systematic error %	4.4	2.2	1.4	5.3	1.7	0.3

Compared with the conventional reverse engineering method, the proposed reconstruction and superposition method have 41% saving in computation time. Future research will be conducted to further optimize the algorithm and incorporate parallel computing.

**Acknowledgements** The authors acknowledge the support from Guangzhou Risong Technology Co. Ltd.

## References

- Brinksmeier E, Mutlugünes Y, Klocke F, Aurich J, Shore P, Ohmori H (2010) Ultra-precision grinding. *CIRP Ann* 59(2):652–671
- Chen Z, Tian L, Fu Y, Xu J, Ding W, Su H (2012) Chip formation of nickel-based superalloy in high speed grinding with single diamond grit. *Int J Abras Technol* 5(2):93–106
- Guo S, Li C, Zhang Y, Wang Y, Li B, Yang M, Zhang X, Liu G (2017) Experimental evaluation of the lubrication performance of mixtures of castor oil with other vegetable oils in MQL grinding of nickel-based alloy. *J Clean Prod* 140:1060–1076
- Javaroni R, Lopes J, Sato B, Sanchez L, Mello H, Aguiar P, Bianchi E (2019) Minimum quantity of lubrication (MQL) as an eco-friendly alternative to the cutting fluids in advanced ceramics grinding. *Int J Adv Manuf Technol* 1–11
- Rodriguez RL, Lopes JC, Hildebrandt RA, Perez RRV, Diniz AE, de Ângelo Sanchez LE, Rodrigues AR, de Mello HJ, de Aguiar PR, Bianchi EC (2019) Evaluation of grinding process using simultaneously MQL technique and cleaning jet on grinding wheel surface. *J Mater Process Technol* 271:357–367
- Lopes JC, Ventura CE, Rodriguez RL, Talon AG, Volpatto RS, Sato BK, de Mello HJ, de Aguiar PR, Bianchi EC (2018) Application of minimum quantity lubrication with addition of water in the grinding of alumina. *Int J Adv Manuf Technol* 97(5–8):1951–1959
- Boswell B, Islam MN, Davies IJ, Ginting Y, Ong AK (2017) A review identifying the effectiveness of minimum quantity lubrication (MQL) during conventional machining. *Int J Adv Manuf Technol* 92(1–4):321–340
- Lopes JC, Ventura CE, Fernandes LM, Tavares AB, Sanchez LE, de Mello HJ, de Aguiar PR, Bianchi EC (2019) Application of a wheel cleaning system during grinding of alumina with minimum quantity lubrication. *Int J Adv Manuf Technol* 102(1–4):333–341
- Lopes JC, de Martini Fernandes L, Domingues BB, Canarim RC, Fonseca MdPC, de Angelo Sanchez LE, de Oliveira RFM, de Mello HJ, Aguiar PR, Bianchi EC (2019) Effect of CBN grain friability in hardened steel plunge grinding. *Int J Adv Manuf Technol* 1–11
- de Mello HJ, de Mello DR, Rodriguez RL, Lopes JC, da Silva RB, de Angelo Sanchez LE, Hildebrandt RA, Aguiar PR, Bianchi EC (2018) Contribution to cylindrical grinding of interrupted surfaces of hardened steel with medium grit wheel. *Int J Adv Manuf Technol* 95(9–12):4049–4057
- Chuang T-j, Jahanmir S, Tang HC (2003) Finite element simulation of straight plunge grinding for advanced ceramics. *J Eur Ceram Soc* 23(10):1723–1733
- Gao K, Chen H, Zhang X, Ren X, Chen J, Chen X (2019) A novel material removal prediction method based on acoustic sensing and ensemble XGBoost learning algorithm for robotic belt grinding of Inconel 718. *Int J Adv Manuf Technol* 105(1–4):217–232
- Chen J, Chen H, Xu J, Wang J, Zhang X, Chen X (2018) Acoustic signal-based tool condition monitoring in belt grinding of nickel-based superalloys using RF classifier and MLR algorithm. *Int J Adv Manuf Technol* 98(1–4):859–872
- Wilson JM, Piya C, Shin YC, Zhao F, Ramani K (2014) Remanufacturing of turbine blades by laser direct deposition with its energy and environmental impact analysis. *J Clean Prod* 80:170–178
- Baptista R, Infante V, Branco C (2008) Study of the fatigue behavior in welded joints of stainless steels treated by weld toe grinding and subjected to salt water corrosion. *Int J Fatigue* 30(3):453–462
- Jin Y (2019) Price M Study on Belt Grinding Performance of Electron Beam Weld of Titanium Alloy. In: Advances in Manufacturing Technology XXXIII: Proceedings of the 17th International Conference on Manufacturing Research, incorporating the 34th National Conference on Manufacturing Research, 10–12 September 2019, Queen's University, Belfast. IOS Press, p 364
- Denkena B, Boess V, Nespor D, Floeter F, Rust F (2015) Engine blade regeneration: a literature review on common technologies in terms of machining. *Int J Adv Manuf Technol* 81(5–8):917–924
- Huang H, Gong Z, Chen X, Zhou L (2002) Robotic grinding and polishing for turbine-vane overhaul. *J Mater Process Technol* 127(2):140–145
- Sun Y, Giblin DJ, Kazerounian K (2009) Accurate robotic belt grinding of workpieces with complex geometries using relative calibration techniques. *Robot Comput Integr Manuf* 25(1):204–210
- Li X, Rong Y (2011) Framework of grinding process modeling and simulation based on microscopic interaction analysis. *Robot Comput Integr Manuf* 27(2):471–478
- Xu X, Chu Y, Zhu D, Yan S, Ding H (2019) Experimental investigation and modeling of material removal characteristics in robotic belt grinding considering the effects of cut-in and cut-off. *Int J Adv Manuf Technol* 1–17
- Qu C, Lv Y, Yang Z, Xu X, Zhu D, Yan S (2019) An improved chip-thickness model for surface roughness prediction in robotic belt grinding considering the elastic state at contact wheel-workpiece interface. *Int J Adv Manuf Technol* 104(5–8):3209–3217
- Han G, Sun M (2008) Optimum path planning of robotic free abrasive polishing process. In: International Conference on Intelligent Robotics and Applications. Springer, pp 906–915
- Wei W, Chao Y (2011) A path planning method for robotic belt surface grinding. *Chin J Aeronaut* 24(4):520–526
- Bian Y, Zhang Y, Gao Z (2013) A path planning method of robotic belt grinding system for grinding workpieces with complex shape surfaces. Paper presented at the international conference on emerging trends in engineering and technology (ICETET), Thailand
- Huang H, Zhou L, Chen X, Gong Z (2003) SMART robotic system for 3D profile turbine vane airfoil repair. *Int J Adv Manuf Technol* 21(4):275–283
- Yilmaz O, Gindy N, Gao J (2010) A repair and overhaul methodology for aeroengine components. *Robot Comput Integr Manuf* 26(2):190–201
- Li L, Li C, Tang Y, Du Y (2017) An integrated approach of reverse engineering aided remanufacturing process for worn components. *Robot Comput Integr Manuf* 48:39–50
- Zhang G, Wang J, Cao F, Li Y, Chen X (2016) 3D curvature grinding path planning based on point cloud data. In: 2016 12th IEEE/ASME International Conference on Mechatronic and Embedded Systems and Applications (MESA). IEEE, pp 1–6
- Li Y, Chen H, Xi N (2017) Automatic Programming for Robotic Grinding Using Real Time 3D Measurement. In: 2017 IEEE 7th Annual International Conference on CYBER Technology in Automation, Control, and Intelligent Systems (CYBER). IEEE, pp 803–808
- Liska J, Vanicek O, Chalus M (2018) Hand-Eye Calibration of a Laser Profile Scanner in Robotic Welding. In: 2018 IEEE/ASME International Conference on Advanced Intelligent Mechatronics (AIM). IEEE, pp 316–321

32. Chen Q (2007) Airborne lidar data processing and information extraction. *Photogramm Eng Remote Sens* 73(2):109
33. Chen J, Paris S, Durand F (2007) Real-time edge-aware image processing with the bilateral grid. In: ACM Transactions on Graphics (TOG), vol 3. ACM, p 103
34. Sithole G, Vosselman G (2005) Filtering of airborne laser scanner data based on segmented point clouds. *International archives of photogrammetry, remote sensing and spatial information sciences* 36 (part 3):W19
35. Lee I-C, Wu B, Li R (2009) Shoreline extraction from the integration of lidar point cloud data and aerial orthophotos using mean-shift segmentation. In: Annual Conference Baltimore, Maryland, ASPRS
36. Balta H, Velagic J, Bosschaerts W, De Cubber G, Siciliano B (2018) Fast statistical outlier removal based method for large 3D point clouds of outdoor environments. *IFAC-PapersOnLine* 51(22): 348–353
37. Ebrahim MA-B (2015) 3D laser scanners' techniques overview. *Int J Sci Res* 4(10):323–331
38. Han X-F, Jin JS, Wang M-J, Jiang W, Gao L, Xiao L (2017) A review of algorithms for filtering the 3D point cloud. *Signal Process Image Commun* 57:103–112
39. Ioannou Y, Taati B, Harrap R, Greenspan M (2012) Difference of normals as a multi-scale operator in unorganized point clouds. In: 2012 Second International Conference on 3D Imaging, Modeling, Processing, Visualization & Transmission. IEEE, pp 501–508
40. Valero S, Chanussot J, Benediktsson JA, Talbot H, Waske B (2010) Advanced directional mathematical morphology for the detection of the road network in very high resolution remote sensing images. *Pattern Recogn Lett* 31(10):1120–1127
41. Clode S, Rottensteiner F, Kootsookos P, Zelniker E (2007) Detection and vectorization of roads from lidar data. *Photogramm Eng Remote Sens* 73(5):517–535
42. Le Saux B, Beaupère A, Boulch A, Brossard J, Manier A, Villemain G (2018) Railway Detection: From Filtering to Segmentation Networks. In: IGARSS 2018–2018 IEEE International Geoscience and Remote Sensing Symposium. IEEE, pp 4819–4822
43. Hu J, Razdan A, Femiani JC, Cui M, Wonka P (2007) Road network extraction and intersection detection from aerial images by tracking road footprints. *IEEE Trans Geosci Remote Sens* 45(12): 4144–4157
44. Lin K, Chen Y, Qiu M, Zeng M, Huang W (2016) SLGC: a fast point-in-area algorithm based on scan-line algorithm and grid compression. In: 2016 11th International Conference on Computer Science & Education (ICCSE). IEEE, pp 352–356
45. Clayton MJ, Warden RB, Parker TW (2002) Virtual construction of architecture using 3D CAD and simulation. *Autom Constr* 11(2): 227–235
46. Keller P, Hering-Bertram M, Hagen H (2012) Surface reconstruction from unorganized 3d point clouds. In: Reverse Engineering—Recent Advances and Applications. IntechOpen

**Publisher's note** Springer Nature remains neutral with regard to jurisdictional claims in published maps and institutional affiliations.